AD_____

Award Number: DAMD17-99-1-9130

TITLE: Finite Element Based Photon Migration Imaging

PRINCIPAL INVESTIGATOR: Huabei Jiang, Ph.D.

CONTRACTING ORGANIZATION: Clemson University
Clemson, South Carolina 29634-5702

REPORT DATE: May 2000

TYPE OF REPORT: Annual Summary

PREPARED FOR: U.S. Army Medical Research and Materiel Command
Fort Detrick, Maryland 21702-5012

DISTRIBUTION STATEMENT: Approved for Public Release;
Distribution Unlimited

The views, opinions and/or findings contained in this report are
those of the author(s) and should not be construed as an official
Department of the Army position, policy or decision unless so
designated by other documentation.

REPORT DOCUMENTATION PAGE

Form Approved
OMB No. 074-0188

Public reporting burden for this collection of information is estimated to average 1 hour per response, including the time for reviewing instructions, searching existing data sources, gathering and maintaining the data needed, and completing and reviewing this collection of information. Send comments regarding this burden estimate or any other aspect of this collection of information, including suggestions for reducing this burden to Washington Headquarters Services, Directorate for Information Operations and Reports, 1215 Jefferson Davis Highway, Suite 1204, Arlington, VA 22202-4302, and to the Office of Management and Budget, Paperwork Reduction Project (0704-0188), Washington, DC 20503

1. AGENCY USE ONLY (Leave blank)	2. REPORT DATE April 2000	3. REPORT TYPE AND DATES COVERED Annual(1 May 99 -30 Apr 00)

4. TITLE AND SUBTITLE
Finite Element Based Photon Migration Imaging

5. FUNDING NUMBERS
DAMD17-99-1-9130

6. AUTHOR(S)
Huabei Jiang, Ph.D.

7. PERFORMING ORGANIZATION NAME(S) AND ADDRESS(ES)
Clemson University
Clemson, South Carolina 29634-5702

E-MAIL:
hjiang@clemson.edu

8. PERFORMING ORGANIZATION REPORT NUMBER

9. SPONSORING / MONITORING AGENCY NAME(S) AND ADDRESS(ES)

U.S. Army Medical Research and Materiel Command
Fort Detrick, Maryland 21702-5012

10. SPONSORING / MONITORING AGENCY REPORT NUMBER

11. SUPPLEMENTARY NOTES

12a. DISTRIBUTION / AVAILABILITY STATEMENT
Approved for public release; distribution unlimited

12b. DISTRIBUTION CODE

13. ABSTRACT (Maximum 200 Words)

This research is aimed at developing a new optical approach, called "Photon Migration Imaging", for breast cancer detection and diagnosis. The project will develop computer software and conduct phantom experiments to achieve the proposed goals. During the first year of this project, we have developed a number of novel schemes that can enhance our current 2D reconstruction software. We have constructed and tested a muti-channel frequency-domain imaging system. We have conducted phantom experiments that confirmed our software enhancement. We have also performed successful fluorescence phantom studies that were proposed to occur during the second year of the project.

14. SUBJECT TERMS

Breast Cancer, Photon Migration Imaging

15. NUMBER OF PAGES
47

16. PRICE CODE

17. SECURITY CLASSIFICATION OF REPORT Unclassified	18. SECURITY CLASSIFICATION OF THIS PAGE Unclassified	19. SECURITY CLASSIFICATION OF ABSTRACT Unclassified	20. LIMITATION OF ABSTRACT Unlimited

NSN 7540-01-280-5500

Standard Form 298 (Rev. 2-89)
Prescribed by ANSI Std. Z39-18
298-102

FOREWORD

Opinions, interpretations, conclusions and recommendations are those of the author and are not necessarily endorsed by the U.S. Army.

_____ Where copyrighted material is quoted, permission has been obtained to use such material.

_____ Where material from documents designated for limited distribution is quoted, permission has been obtained to use the material.

_____ Citations of commercial organizations and trade names in this report do not constitute an official Department of Army endorsement or approval of the products or services of these organizations.
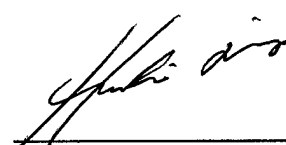
N/A In conducting research using animals, the investigator(s) adhered to the "Guide for the Care and Use of Laboratory Animals," prepared by the Committee on Care and use of Laboratory Animals of the Institute of Laboratory Resources, national Research Council (NIH Publication No. 86-23, Revised 1985).

N/A For the protection of human subjects, the investigator(s) adhered to policies of applicable Federal Law 45 CFR 46.

N/A In conducting research utilizing recombinant DNA technology, the investigator(s) adhered to current guidelines promulgated by the National Institutes of Health.

N/A In the conduct of research utilizing recombinant DNA, the investigator(s) adhered to the NIH Guidelines for Research Involving Recombinant DNA Molecules.

N/A In the conduct of research involving hazardous organisms, the investigator(s) adhered to the CDC-NIH Guide for Biosafety in Microbiological and Biomedical Laboratories.

_____   5/23/00
PI - Signature   Date

Table of Contents

Introduction

The ability of near-infrared (NIR) light-based techniques to noninvasively image and analyze tissue structure and function promises their great potential for detection and diagnosis of breast cancer. Optical diagnostic techniques allow us to not only enhance the existing capabilities, but to eliminate the need for physical biopsies. In addition, optical imaging is inexpensive and portable, which indicates that optical imaging could be an ideal candidate for routine breast screening. However, since the scattering properties of tissues convolute re-emitted NIR signals, the extraction of pertinent information continues to remain elusive. An understanding of light propagation and light-tissue interaction is required before the optical technologies can substantially impact diagnostic medicine.

Research efforts in the Biomedical Optics Laboratory at Clemson University are focused on the biophysics of light propagation and light-tissue interaction in order to engineer appropriate approaches for noninvasive breast imaging and spectroscopy. Specifically, we are developing indirect optical/fluorescence approaches using photon migration measurements in the continuous-wave and frequency domains. These indirect optical/fluorescence approaches or image reconstructions are computationally based on the powerful finite element methods. A CCD-based optical spectroscopic imaging system is already operational in our laboratory for continuous-wave tomographic photon migration measurements, while a frequency-domain system is still under construction. Using these optical systems coupled with our finite element based reconstruction algorithms, we will be able to extract spatial/spectroscopic maps of tissue optical properties, lifetime and/or yield of endogenous and exogenous fluorescent probes. Since metabolic tissue states can be identified by our approaches, diagnostic information is also obtained in addition to detection of tumor.

This Career Development application for support of Dr. Huabei Jiang will facilitate the establishment/continuation of these research activities. Interdisciplinary interactions with the Greenville Hospital System (Greenville, SC) will be enhanced, which insures the direction of research towards a clinically pertinent and feasible system.

Body

This report describes work accomplished during the first year of a proposed four-year study. This Career Award supports Dr. Jiang's research on optical and fluorescence imaging using both continuous-wave and frequency-domain measurements. The focus of the proposed work in Year 1 is the implementation of some enhancing schemes in our existing 2D reconstruction codes as well as some preparation for phantom studies. This will pave the way for us to conduct 2D image reconstruction in Year 2 for simple experimental configurations with dye-free phantom background.

Software work: while we have implemented some of the proposed image enhancing schemes in the current 2D codes including the total variation minimization, weighted least squares criterion and low pass filtering, we have also developed two additional novel schemes that were not proposed originally. Our existing algorithms require an additional calibration measurement with a homogeneous phantom in order to determine

the excitation source strength and the boundary conditions coefficient that are critical for a successful reconstruction. The first scheme, which uses the idea of normalizing the photon density in the reconstruction algorithm, allows for the reconstruction of optical property images without measuring the excitation source strength. The second scheme, which is based on a simple least-squares minimization between the measured and computed photon densities at the boundary, can provide us the boundary conditions coefficient. The normalizing scheme-based algorithm eliminates the need of absolute measurement data for reconstruction, yet provides us absolute quantitative optical images. We have tested these two schemes using simulations in which noise-free and noisy "measured" data are applied. We have also confirmed these simulations using tissue-like phantom experiments (see *Phantom Experiments* section below). For the detail of the two enhancing schemes and the simulation and experimental results, see a manuscript entitled "Enhancing Diffusion Optical Tomography through A Normalizing Reconstruction Algorithm and A Simple Least-Squares Minimization Scheme" provided in the *Appendix* to the Summary Report.

Hardware Development: in order to conduct the proposed fluorescence lifetime imaging work, we must first construct a frequency-domain optical system. Support from NIH and Greenville Hospital System has allowed us to complete this system. We have built a 16x16 channel automatic frequency-domain imaging system that allows us to collect tomographic data within eight minutes at the present time. The system has been described in detail in a second manuscript entitled "Development of a combined optical and fluorescence imaging system in frequency-domain for breast cancer detection" provided in the *Appendix* to the Summary Report.

Phantom Experiments: using the developed frequency-domain imaging system, we have conducted a series of phantom experiments to confirm the two new image enhancing schemes. The successful results have been presented in the first manuscript included in the *Appendix*. In addition, we have begun to conduct phantom experiments for fluorescence lifetime reconstruction which was proposed to take place during the second year of the project. In these experiments, we present successful quantitative simultaneous reconstruction of both lifetime and yield images from frequency-domain measurements using indocyanine green (ICG) dye and tissue-like phantoms. To our knowledge, the results shown here are the first experimentally reconstructed images for which simultaneous recovery of both lifetime and yield profiles has been achieved with absolute ac excitation and fluorescence data. We show the ability of our algorithm to reconstruct images in which single- and multi-target are embedded in a circular background. Our experimental setup used was the automated multi-channel frequency-domain system mentioned above. The system employed a radio-frequency intensity-modulated near-infrared beam. The laser beam at 785 nm was sent to the phantom by 16 fiber optic bundles coupled with a high precision moving stage. The diffused radiation was received by another 16 channel fiber optic bundles and delivered to a PMT. A second PMT was used to record the reference signal. These PMTs were supplied at a radio-frequency modulated current with 0.1-1KHz shift. The intermediary frequency signal obtained from the PMTs was processed using a National Instruments board. To increase the dynamic range of intensities that the PMT can detect, an automated filter wheel with pre-calibrated neutral density filters was added to the system. For every source position, 16 measurements for each detector were made, taking alternatively 100 ms samples for sample and reference signals. Fluorescence

signals were obtained through an 830nm interference filter placed in front of the detection PMT. ac intensity and phase shift between reference and sample signals were obtained using FFT Labview routines. The total data collection time for 256 measurements was 8 minutes.

In our experiments we used a 50 mm diameter solid phantom (0.5% Intralipid +India ink+Agar) as the background medium, making the absorption coefficient $\mu_a = 0.0005/mm$, and the reduced scattering coefficient $\mu'_s = 0.5/mm$. Both single- and two-target configurations were used. The solid targets contained ICG dye with different concentrations (0.5 or 1 μM) plus 0.5% Intralipid and Agar (perfect uptake of the dye was considered here, i.e., no dye was present in the background). The single target had 12.6 or 7.8 mm in diameter, while both targets had 10.3 mm for the two-target case. The 2D finite-element mesh used had 249 nodes and 448 elements for both forward and inverse solutions. The image results have been presented in a third manuscript entitled "Fluorescence lifetime tomography of heterogeneous turbid media using frequency-domain measurements" provided in the *Appendix* to this Summary Report.

We have shown that we are able to obtain simultaneous reconstruction of both lifetime and yield images in turbid media using ac excitation and fluorescent data. While an ideal, perfect uptake of fluorescent dye in the target has been assumed, this study has clearly demonstrated the feasibility of fluorescence lifetime imaging in turbid media using the reconstruction approach described here. To add fluorophores into the background would primarily challenge our hardware system since the fluorescent signals would be weakened in this case. However, we do not anticipate considerable difficulty to obtain enough signal-to-noise ratio for reconstruction when the fluorophores are present in the background since the dye uptake ratio between the tumor and normal tissue can be as high as 10:1. In this regard, we plan to conduct experiments in Years 2-3 of this project.

Key Research Accomplishments

1. We have developed a number of novel schemes that can enhance our current 2D reconstruction software.
2. We have constructed and tested a muti-channel frequency-domain imaging system.
3. We have conducted phantom experiments that confirmed our software enhancement. We have also performed successful fluorescence phantom studies that were proposed to occur during the second year of the project.

Reportable Outcomes (see the Appendix to this Summary Report)

Conclusions

We have made a significant progress that has exceeded the statement of work proposed for Year 1 of this project. Given the successful first year, we will be able to fulfil or exceed the work statement for Year 2, and we will carry these successful works over into the final year of this project.

Appendix

1. H. Jiang, S. Liao, N. Iftimia, "Enhancing Diffusion Optical Tomography through A Normalizing Reconstruction Algorithm and A Simple Least-Squares Minimization Scheme", *Journal of Optical Society of America A* (in press), 2000.

2. N. Iftimia, S. Liao, H. Jiang, "Development of a combined optical and fluorescence imaging system in frequency-domain for breast cancer detection", *Proc. OSA Biomedical Meetings*, 383-385(2000).

3. H. Jiang, Y. Yang, N. Iftimia, "Fluorescence lifetime tomography of heterogeneous turbid media using frequency-domain measurements", *Optics Letters* (submitted), 2000.

Enhancing Diffusion Optical Tomography through A Normalizing Reconstruction Algorithm and A Simple Least-Squares Minimization Scheme

Huabei Jiang*, Supeng Liao, and Nicusor Iftimia

Department of Physics and Astronomy

Clemson University

Clemson, SC 29634-0978

*To whom correspondence should be addressed

Abstract

In this paper, we present two schemes that can enhance our established finite-element based optical image reconstruction algorithms. Our existing algorithms require an additional calibration measurement with a homogeneous phantom in order to determine the excitation source strength and the boundary conditions coefficient that are critical for a successful reconstruction. The first scheme, which uses the idea of normalizing the photon density in the reconstruction algorithm, allows for the reconstruction of optical property images without measuring the excitation source strength. The second scheme, which is based on a simple least-squares minimization between the measured and computed photon densities at the boundary, can provide us the boundary conditions coefficient. The normalizing scheme-based algorithm eliminates the need of absolute measurement data for reconstruction, yet provides us absolute quantitative optical images. We test these two schemes using simulations in which noise-free and noisy "measured" data are applied. We further confirm these simulations using tissue-like phantom experiments.

1. Introduction

There has been considerable interest in the application of diffusion optical tomography for tissue diagnostics as evidenced by recent feature issues on this topic[1-3]. Among various imaging approaches under developing, diffusion optical tomography based on reconstruction algorithms has received particular attention since it can offer both structural and functional information of tissue[4-17]. This unique capability may allow for non-invasively differentiating between benign and malignant tumor, for example. In this regard, the core task is to develop an effective reconstruction algorithm for forming an image of the spatial distribution of tissue optical absorption and scattering properties.

We have presented a finite-element based reconstruction algorithm[18], which has been evaluated using extensive simulated and experimental data in the last few years[7,18-22]. These studies clearly suggest that we have identified a powerful framework with which to pursue quantitative image reconstruction of both absorption and scattering property profiles. A calibration procedure was used in all of the experimental imaging studies performed, however. In this procedure, we used homogeneous medium measurements to calibrate the source term and the boundary conditions (BCs)[7,19]. Although it was straightforward to do it, a trial-and-error process was needed to complete this calibration procedure. We found that the amplitude of the source largely determined the computed photon density amplitude and BCs could affect the computed overall light distribution considerably, which suggests that this time-consuming procedure may introduce significant errors to the reconstruction if not carefully done. In particular, this calibration procedure may not be viable for *in vivo* data[22].

In this paper, we present two schemes that can enhance our established finite-element based optical image reconstruction algorithms. The first scheme, which uses the idea of

3

normalizing the photon density in the reconstruction algorithm, allows for the reconstruction of optical property images without measuring the excitation source strength. The second scheme, which is based on a simple least-squares minimization between the measured and computed photon densities at the boundary, can provide us the boundary conditions coefficient. The normalizing scheme-based algorithm eliminates the need of absolute measurement data for reconstruction, yet provides us absolute quantitative optical images. We perform numerical simulations to test the two schemes where noise-free and noisy "measured" data are applied. We confirm these simulations using tissue-like phantom experiments.

2. Normalizing Scheme

Our image reconstruction algorithm has been based on the 2D diffusion approximation[18,19]. For cw light illumination, the steady-state diffusion equation can be stated as

$$\nabla \cdot D(r)\nabla\Phi(r) - \mu_a(r)\Phi(r) = -S(r) \tag{1}$$

where $\Phi(r)$ is the photon density, $D(r)$ is the diffusion coefficient, and $\mu_a(r)$ is the absorption coefficient. The diffusion coefficient can be written as

$$D(r) = \frac{1}{3[\mu_a(r) + \mu_s'(r)]} \tag{2}$$

where $\mu_s'(r)$ is the reduced scattering coefficient, S_0 is the source term in (1) which for a point source can be written as $S = S_0\delta(r - r_0)$, where S_0 is the source strength and $\delta(r - r_0)$ is the Dirac delta function for a source at r_0.

2.1. Non-normalizing Reconstruction Algorithm

Our non-normalizing reconstruction algorithm (in short, Non-NRA) has been described in details in Ref. 18. Here we just provide an overview in order to present the normalizing

reconstruction algorithm (in short, NRA). Following the procedures outlined by Paulsen and Jiang[18], we can obtain a finite element discretization of (1)

$$(A - \alpha B)\Phi = C \qquad (3)$$

where the elements of matrix A are $a_{ij} = \left\langle -\sum_{k=1}^{K} D_k \phi_k \nabla \phi_j \cdot \nabla \phi_i - \sum_{\ell=1}^{L} \mu_\ell \phi_\ell \phi_j \phi_i \right\rangle$ where $\langle \ \rangle$

indicates integration over the problem domain; the elements of matrix B are $b_{ij} = \sum_{j=1}^{M} \Phi_j \oint \phi_j \phi_i ds$

where $\Phi = [\Phi_1, \Phi_2, \cdots \Phi_N]^T$, Φ_i is the photon density at node i, N is the number of nodes in

the finite elements mesh, M is the number of boundary measurements, $\oint$ expresses integration

over the boundary surface where type III boundary conditions (BCs), $-D\nabla\Phi \cdot \hat{n} = \alpha\Phi$, have

been applied; α is a parameter relating to the internal reflection at the boundary; the elements of

vector C are $\langle -S\phi_i \rangle$. In (3), Φ, D and μ_a have been expanded as the sum of coefficients

multiplied by a set of locally spatially varying Lagrange polynomial basis functions $\phi_j, \phi_k, \phi_\ell$.

Note that the expansions used to represent the diffusion and absorption coefficient profiles in (3)

are K and L terms long where $K \neq L \neq N$ in general; however, in the work reported here K = L

= N.

Based on a Newton's iterative scheme as described by Paulsen and Jiang[18], the following

matrix equation can be obtained for providing the inverse solution of interest

$$(\mathfrak{I}^T \mathfrak{I} + \lambda I)\Delta\chi = \mathfrak{I}^T [\Phi^{(m)} - \Phi^{(c)}] \qquad (4)$$

where $\Delta\chi = (\Delta D_a, \Delta D_2, \cdots, \Delta D_N, \Delta\mu_{a,1}, \Delta\mu_{a,2}, \cdots, \Delta\mu_{a,N})^T$ is the updates of the diffusion and

absorption coefficient profiles; χ represents either D or μ_a; $\mathfrak{I}$ is the Jacobian matrix which

consists of derivatives of the photon density with respect to χ and $\mathfrak{I}^T$ is the transpose of $\mathfrak{I}$,

$\Phi^{(m)}$ and $\Phi^{(c)}$ are measured and computed photon densities respectively; λ is a regularization parameter which is used to regularize or stabilize the decomposition of $\mathfrak{I}^T\mathfrak{I}$ and I is a unit matrix.

The elements of the Jacobian matrix are computed from the following matrix relationship, which is the differentiation of equation (3)

$$(A - \alpha B)\frac{\partial \Phi}{\partial \chi} = \frac{\partial C}{\partial \chi} - \Phi \frac{\partial A}{\partial \chi} \qquad (5)$$

Evaluation of (4) for the update vector χ requires the solutions of (3) and (5), which depend on the current estimate of χ. Once the update vector has been computed, a new χ vector becomes available and the procedure is repeated until a converged value of the difference norm between the measured and computed data is reached. Note that, when reconstructing 2D images from experimental data using this Non-NRA, both the source term, S, and the boundary conditions coefficient, α, need to be determined through a calibration procedure with a homogenous phantom[7,19].

2.2. Normalizing Algorithm

Based on (3) and (5), we derive a normalizing reconstruction algorithm. Assume that Φ_0 is a known measurement at a node on the boundary. Dividing Φ_0 at the both sides of equation (3), we can obtain a normalized form of equation (3)

$$(A - \alpha B)\frac{\Phi}{\Phi_0} = \frac{C}{\Phi_0} \qquad (6)$$

Similarly, a normalized differentiation of matrix equation (5) leads to

$$(A - \alpha B)\frac{\partial}{\partial \chi}\left(\frac{\Phi}{\Phi_0}\right) + \left(\frac{\Phi}{\Phi_0}\right)\frac{\partial A}{\partial \chi} = \frac{1}{\Phi_0}\frac{\partial C}{\partial \chi} + C\frac{\partial}{\partial \chi}\left(\frac{1}{\Phi_0}\right) \qquad (7)$$

(7) can be rearranged as follows

$$(A - \alpha B)\frac{\partial}{\partial \chi}\left(\frac{\Phi}{\Phi_0}\right) = \left(\frac{1}{\Phi_0}\right)\left(\frac{\partial C}{\partial \chi} - \Phi \frac{\partial A}{\partial \chi}\right) - \frac{C}{\Phi_0^2}\frac{\partial \Phi_0}{\partial \chi} \qquad (8)$$

where again χ represents either D or μ_a.

By comparing (3) and (5) to (6) and (8), we can easily obtain the elements of the normalized Jacobian's matrix which are needed to construct the normalized form of (4). Since the equations (5) and (8) originate from the same diffusion equation (3), both non-normalizing and normalizing algorithms should provide the same reconstruction of the optical properties. The main advantage of NRA over Non-NRA is that the former is independent of source intensity. In other words, we need not calibrate the source term in measurements under experimental or clinical conditions, which usually is a time-consuming procedure and may cause additional errors in measured data. In Section 4, we will confirm our NRA scheme by using simulations and experiments.

3. Least-Squares Minimization Scheme

We use a simple least-squares minimization scheme to determine the boundary conditions coefficient, α. That is, we compute the following X^2 value as a function of α,

$$X^2 = \sum_{i=1}^{M}\left(\Phi_i^{(m)} - \tilde{\Phi}_i^{(c)}\right)^2 \qquad (9)$$

where M is the number of boundary measurements; $\Phi^{(m)}$ is the measured photon density from a given experimental inhomogeneous medium (a phantom or *in vivo* tissue), and $\tilde{\Phi}_i^{(c)}$ is the computed photon density from a numerical simulation homogeneous medium with the same geometry as the experimental medium. We argue that the minimum of X^2 corresponds to the

7

correct value of α associated with the experimental inhomogeneous medium. This argument is confirmed in the following section using simulations and experiments.

4. Experimental Materials and Methods

Our experimental setup is an automated multi-channel frequency-domain system that has been described in detail elsewhere.[23] In this system, a radio-frequency intensity-modulated near-infrared beam at 785 nm is sent to the phantom by 16 fiber optic bundles coupled with a high precision moving stage. The diffused light is received by another 16 channel fiber optic bundles and delivered to a PMT. A second PMT is used to record the reference signal. These PMTs are supplied at a radio-frequency modulated current with 0.1-1KHz shift. The intermediary frequency signal obtained from the PMTs is processed using a National Instruments board. To increase the dynamic range of intensities that the PMT can detect, an automated filter wheel with pre-calibrated neutral density filters is added to the system. For every source position, 16 measurements for each detector are made, taking alternatively 100 ms samples for sample and reference signals. dc, ac and phase shift between reference and sample signals are obtained using FFT Labview routines. The total data collection time for 256 measurements is 8 minutes. We just used measured dc data to reconstruct the absorption and scattering images in this study.

In our experiments we used a 50 mm diameter cylindrical solid phantom (1% Intralipid+India ink+Agar) as the background medium, making the absorption coefficient, $\mu_a = 0.005/\text{mm}$ and the reduced scattering coefficient, $\mu_s' = 1.0/\text{mm}$. Both single- and two-target configurations were used. In the single-target case, a target with 15.0 mm in diameter was examined. In the two-target case, one 8.0 mm and one 12.5 mm diameter target were embedded in the background. μ_a of the target varied from 0.020/mm to 0.040/mm; μ_s' of the target was the same as that of the background. These values of the background and target optical properties are

8

similar to those for normal and tumor breast tissues.[24] The 2D finite-element mesh used had 249 nodes and 448 elements for both forward and inverse solutions. Note that here we do not need to use the dual mesh scheme as used before[21,22] in order to obtain quantitative reconstruction by dc data. All the reconstructions were performed in a 400 MHz Pentium II PC.

5. Results

In this section, we will evaluate the above NRA and the simple least-squares minimization scheme using simulated and experimental data. The parameters used in the experiments have been given in Section 4. For simulations, the background geometry and optical properties were exactly the same as that for experiments. A single target with a radius of 10 mm was embedded in the background. The optical properties in the target were $\mu_a = 0.01/\,mm$ and $\mu_s' = 2.0/\,mm$. The mesh used had 241 nodes and 460 triangular elements. A circular symmetric configuration of 16 source and 16 detectors were used, providing a set of 256 "measured" data. Assume that the data is noise free and has 5% noise respectively, we have tested both NRA and Non-NRA for comparison. For the reconstructions using NRA, we selected the maximum value of the photon densities at the boundary to normalize each set of "measured" data. To determine the boundary conditions coefficient, α, we computed the X^2 as function of α.

Figs. 1 and 2 show the reconstructed images using Non-NRA and NRA in which 0% and 5% noise were added to the "measured" data, respectively. When different source intensity values were used, all the images for both μ_a and μ_s' reconstructed using NRA scheme are exactly the same as the images shown in Fig. 1(c) and (d) under the condition of 0% noise and in Fig. 2 (c) and (d) under the condition of 5% noise. For this reason, these images with different source intensities are not presented here. Table 1 gives the quantitative information about the RMS errors for the images shown in Figs. 1-2. The image RMS errors are defined as

$\sqrt{1/N \sum_{i=1}^{N} [(\chi_{exact} - \chi_{reconstructed})/\chi_{exact}]^2}$ where N is the number of sample positions and χ is either μ_a or μ'_s.

In Fig. 3 (a), X^2 is depicted as a function of α without noise added to the "measured" data when the optical properties used for computing $\tilde{\Phi}_i^{(c)}$ are the same as the background values, 2%-off the background values, and 20%-off the background values, respectively. Fig. 3 (b) presents the same results as Fig. 3 (a) except that 5% noise was added to the "measured" data. Note that the exact value of α used here is 0.7.

Fig. 4 displays X^2 versus α for the two sets of experimental data. As can be seen, a minimum value of the X^2 error is clearly reached at $\alpha = 0.57$ for the single target case and at $\alpha = 0.52$ for the two target case. Using these derived values of α, the absorption and scattering images were reconstructed and are shown in Fig. 5 for both experimental configurations. As evidenced, the images are clearly recovered.

6. Discussion and Conclusions

The results presented in the previous section confirm the NRA scheme outlined in Section 2. It is clear that the reconstructions of both μ_a and μ'_s images using NRA are independent of the excitation source intensity. As can be seen from Figs.1 and 2, when no noise was added to the "measured" data, the visual quality, in terms of the target shape and size, of μ_a images reconstructed using Non-NRA and NRA is about the same, while the visual quality of μ'_s image recovered by NRA is even better than that by Non-NRA. Most interestingly, when 5% noise was added to the "measured" data, we obtained much better reconstructed images for both μ_a and μ'_s using NRA than that using Non-NRA in terms of the target shape and size recovered. This suggests that NRA is less sensitive to the noise effect than Non-NRA for reconstructing

10

both μ_a and μ_s' images. It is also interesting to note that the overall recovery of the target shape and size for μ_a images is better than that for μ_s' images, no matter Non-NRA or NRA is used.

Table 1 presents the average values and the RMS errors of optical properties recovered. In terms of the average optical property values, Non-NRA and NRA gave similar accuracies in most cases except that NRA provided a better value of μ_s' than Non-NRA for the target under the condition of 5% noise ($\mu_s'=1.64$ from NRA whereas $\mu_s'=1.27$ from Non-NRA). In terms of the RMS errors, overall Non-NRA provided slightly better results than NRA for both μ_a and μ_s' under the condition of 0% noise. However, under the condition of 5% noise, neither Non-NRA nor NRA showed consistent better results than its counterpart. The relative high RMS errors in some of the cases here were caused by the relative high or low values of μ_a or μ_s' at some locations. These relatively high or low values of μ_a or μ_s' can be easily smoothed by using a low pass filtering[19,21], which would provide much lower RMS errors.

No matter 0% or 5% was added to the "measured" data, Fig. 3 shows that X^2 reaches its single minimum right at the exact value of $\alpha=0.7$, when the optical property values used for computing $\tilde{\Phi}_i^{(c)}$ are the same as the background, or just off 2%. The minimum occurs at $\alpha=0.64$ when the optical property values used for computing $\tilde{\Phi}_i^{(c)}$ are off 20% relative to that of the background under both the conditions of 0% and 5% noise. Clearly the amount of noise added to the "measured" data does not appear to affect the determination of α. The optical property values used for computing $\tilde{\Phi}_i^{(c)}$ are the single important factor impacting this determination. Given the fact that the optical properties for the normal background tissue as *a priori* are typically known with an accuracy better than 10% error[24-26], we argue that the method described here offers a viable way for determining α in an *in vivo* setting. We have found that a significant

11

shift of α value (about $\alpha=0.45$) presented when the optical property values used for computing $\tilde{\Phi}_i^{(c)}$ are 100%-off the background optical property values.

From experimental data, Fig. 4 shows that X^2 reaches the single minimum at $\alpha=0.57$ and $\alpha=0.52$ for the single and two target cases, respectively. The exact values of α are not available since it is difficult for us to obtain such values given our experimental conditions. Theoretically these values would depend upon the ratio of the refractive indexes of the phantom or tissue and air or surrounding medium.[27,28] In our experiments, most of the boundary space was surrounded by the thirty-two 3 mm source/detection optic fibers. This means that the surrounding medium used in our study was a combination of the optic fibers and air (about 75% of the medium was fibers and 25% was air). Since the refractive index of the glass optic fibers is about 1.53, this would give us an effective index of 1.40 for the mixed medium which is larger than that of the phantom used (1.33 for the Intralipid phantom used). Based on the empirical formula provided in Refs. 27 and 28, α can be calculated to be 0.63 for the estimated boundary surrounding. Our derived values of α appear to have a good agreement with this estimated actual value. Since a mixed surrounding medium is often used in reality for optical tomography, our method offers a practical way to handle the complex experimental boundary conditions. The small difference in α values for the single and two target cases are due to the difference in the composition of the phantom materials used in each case. With the derived α values, we obtained the optimal reconstructed images shown in Fig. 5. As can be seen, both single and two targets can be clearly detected quantitatively in terms of the optical property value, size and location of the targets.

In summary, we have developed two schemes that can enhance our established reconstruction algorithms. The described normalizing scheme-based algorithm allows for

reconstruction of optical property images without the calibration procedure with respect to the excitation source. Furthermore, our simulated results show that the normalizing scheme-based algorithm is even more resistant to the noise effect than the reconstruction algorithm without a normalizing scheme. We have also demonstrated that the use of a simple least-squares minimization scheme can provide us the correct boundary conditions coefficient that is important for a successful reconstruction. Our simulations and experiments indicate that the concurrent use of the two schemes can eliminate the calibration procedure that was previously needed when dealing with experimental data. Although we have chosen cw illumination as our test case in this study, the proposed schemes can be easily adapted for reconstructions in frequency- or time-domain.

References

1. B. W. Pogue, "Diffusion optical tomography: introduction", *Opt. Express* **4**, 1(1999).

2. B. Tromberg, A. Yodh, E. Sevick-Muraca, D. Pine, "Diffusing photons in turbid media: introduction", *Appl. Opt.* **36**, 9(1997).

3. A. Yodh, B. Tromberg, E. Sevick-Muraca, D. Pine, "Diffusing photons in turbid media: introduction", *J. Opt. Soc. Am. A* **14**, 136(1997).

4. R. L. Barbour, H. Graber, J. Chang, S. Barbour, P. Koo, R. Aronson, "MRI-guided optical tomography: Prospects and computation for a new imaging method", *IEEE Computational Science & Engineering* **2**, 63-77(1995).

5. S. R. Arridge and M. Schweiger, "Image reconstruction in optical tomography", *Phil. Trans. R. Soc. Lond. B* **352**, 717-726(1997).

6. M. A. O'Leary, D. A. Boas, B. Chance, and A. G. Yodh, "Experimental images of heterogeneous turbid media by frequency-domain diffusing-photon tomography," *Opt. Lett.* **20**, 426-428(1995).

7. H. Jiang, K. D. Paulsen, U. L. Osterberg, B. W. Pogue, and M. S. Patterson, "Simultaneous reconstruction of absorption and scattering profiles in turbid media from near-infrared frequency-domain data," *Opt. Lett.* **20**, 2128-2130(1995).

8. H. Jiang, "Optical image reconstruction based on the third-order diffusion equations", *Opt. Express* **4**, 241-246(1999).

9. W. Cai, S. Gayen, M. Xu, M. Zevallos, M. Alrubaiee, M. Lax, R. Alfano, "Optical tomographic image reconstruction from ultrafast time-sliced transmission measurements", *Appl. Opt.* **38**, 4237-4246(1999).

10. S. B. Colak, D. Papaioannou, G. tHooft, M. vander Mark, H. Schomberg, J. Paasschens, J. Melissen, N. van Asten, "Tomographic image reconstruction from optical projections in light diffusing media", *Appl. Opt.* **36**, 180-213(1997).

11. S. A. Walker, S. Fantini, E. Gratton, "Image reconstruction by backprojection from frequency-domain optical measurements in highly scattering media"" *Appl. Opt.* **36**, 170-179(1997).

12. B. W. Pogue, T. McBride, J. Prewitt, U. Osterberg, K. Paulsen, "Spatially variant regularization improves diffuse optical tomography", *Appl. Opt.* **38**, 2950-2961(1999).

13. C. L. Matson, H. Liu, "Analysis of the forward problem with diffuse photon density waves in turbid media by use of a diffraction tomography model", *J. Opt. Soc. Am. A* **16**, 455-466(1999).

14. J. Scotland, "Continuous-wave diffusion imaging", *J. Opt. Soc. Am. A* **14**, 275-279(1997).

15. X. Cheng, D. Boas, "Diffuse optical reflection tomography with continuous-wave illumination", *Opt. Express* **3**, 118-123(1998).

16. M. J. Eppstein, D. Dougherty, T. Troy, E. Sevick-Muraca, "Biomedical optical tomography using dynamic parameterization and Bayesian conditioning on photon migration measurements", *Appl. Opt.* **38**, 2138-2150(1999).

17. J. C. Ye, K. Webb, R. Millane, T. Downar, "Modified distorted Born iterative method with an approximate Frechet derivative for optical diffusion tomography", *J. Opt. Soc. Am. A* **16**, 1814-1826(1999).

18. K. D. Paulsen and H. Jiang, "Spatially-varying optical property reconstruction using a finite-element diffusion equation approximation," *Med. Phys.* **22**, 691-702(1995).

19. H. Jiang, K. Paulsen and U. Osterberg, B. Pogue and M. Patterson, "Optical image reconstruction using frequency-domain data: simulations and experiments", *J. Opt. Soc. Am. A* **13**, 253-266(1996).

20. H. Jiang, K. Paulsen and U. Osterberg, "Optical image reconstruction using DC data: simulations and experiments", *Phys. Med. Biol.* **41**, 1483-1498(1996).

21. H. Jiang, K. Paulsen, U. Osterberg and M. Patterson, "Frequency-domain optical image reconstruction in heterogeneous media: an experimental study of single-target detectability", *Appl. Opt.* **36**, 52-63(1997).

22. H. Jiang, K. Paulsen, U. Osterberg and M. Patterson, "Frequency-domain near-infrared photo diffusion imaging: initial evaluation in multi-target tissue-like phantoms", *Med. Phys.* **25**, 183-193(1998).

23. N. Iftimia, S. Liao, H. Jiang, "Development of a combined optical and fluorescence imaging system in frequency-domain for breast cancer detection", *Proc. OSA Biomedical Topical Meetings*, 383-385(2000).

24. B. J. Tromberg, O. Coquoz, J. Fishkin, T. Pham, E. Anderson, J. Butler, M. Cahn, J. Gross, V. Venugopalan, D. Pham, "Non-invasive measurements of breast tissue optical properties using frequency-domain photon migration", *Phil. Trans. R. Soc. Lond. B* **352**, 661-668(1997).

25. S. J. Matcher, M. Cope, D. Delpy, "In vivo measurements of the wavelength dependence of tissue-scattering coefficients between 760 and 900 nm measured with time-resolved spectroscopy", *Appl. Opt.* **36**, 386-396(1997).

26. J. B. Fishkin, O. Coquoz, E. Anderson, M. Brenner, B. Tromberg, "Frequency-domain photon migration measurements of normal and malignant tissue optical properties in a human subject", *Appl. Opt.* **36**, 10-20(1997).

27. T. J. Farrell, M. S. Patterson, B. C. Wilson, "A diffusion theory model of spatially resolved, steady-state diffuse reflectance for the noninvasive determination of tissue optical properties *in vivo*," *Med. Phys.* **19,** 879-888 (1992)

28. R. A. J. Groenhuis, H. Ferwerda, and J. Ten Bosch, "Scattering and absorption of turbid materials determined from reflection measurements. 1: Theory," *Appl. Opt.* **22**, 2456-2462 (1983)

Figure Captions

Figure 1. Images reconstructed by non-normalizing algorithm (Non-NRA) and normalizing algorithm (NRA) from simulated data without noise added to the "measured" data. (a) μ_a image by Non-NRA; (b) μ_s' image by Non-NRA; (c) μ_a image by NRA; (d) μ_s' image by NRA.

Figure 2. Images reconstructed by non-normalizing algorithm (Non-NRA) and normalizing algorithm (NRA) from simulated data with 5% noise added to the "measured" data. (a) μ_a image by Non-NRA; (b) μ_s' image by Non-NRA; (c) μ_a image by NRA; (d) μ_s' image by NRA.

Figure 3. (a) X^2 as a function of α calculated without noise added to the "measured" data. Three sets of optical property values were used for computing X^2: (1) 0%-off the background values (the solid line), (2) 2%-off the background values (the dash-dotted line), and (3) 20%-off the background values (the dashed line). (b) The same as (a) except that 5% noise was added to the "measured" data.

Figure 4. X^2 versus α for experimental data when both single and two target configurations were used.

Figure 5. Reconstructed images with experimental data. (a) μ_s' image for the single target case. (b) μ_a image for the single target case. (c) μ_s' image for the two target case. (d) μ_a image for the two target case.
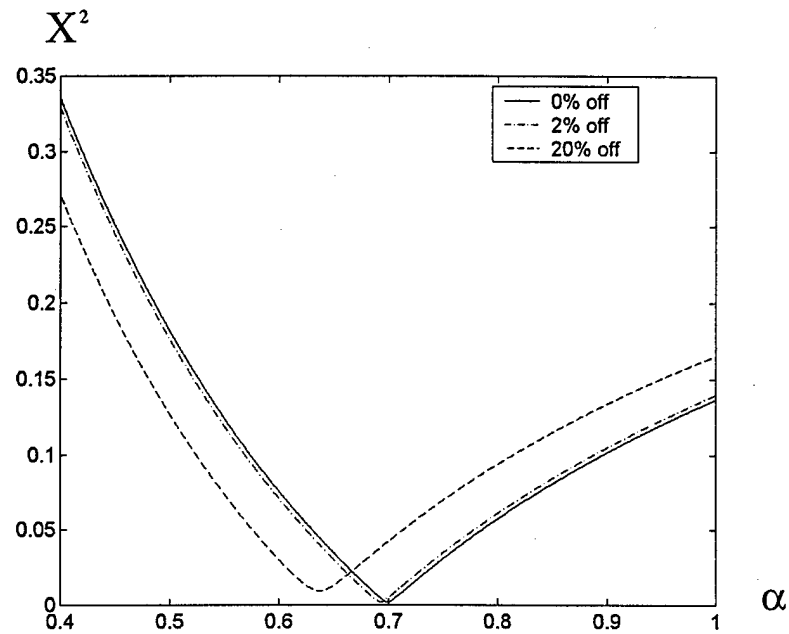
(a)

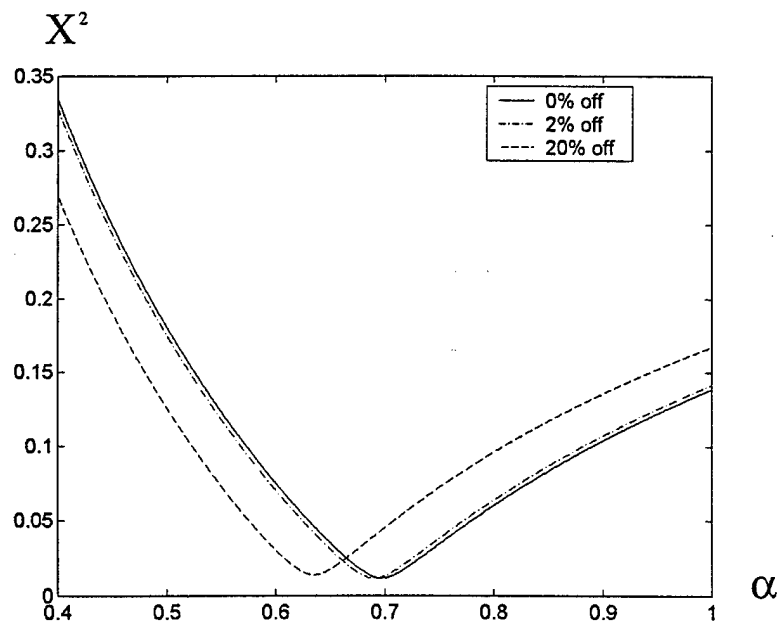(b)

(c)

(d)

Fig. 1 — Jiang

(a)

(b)

(c)

(d)
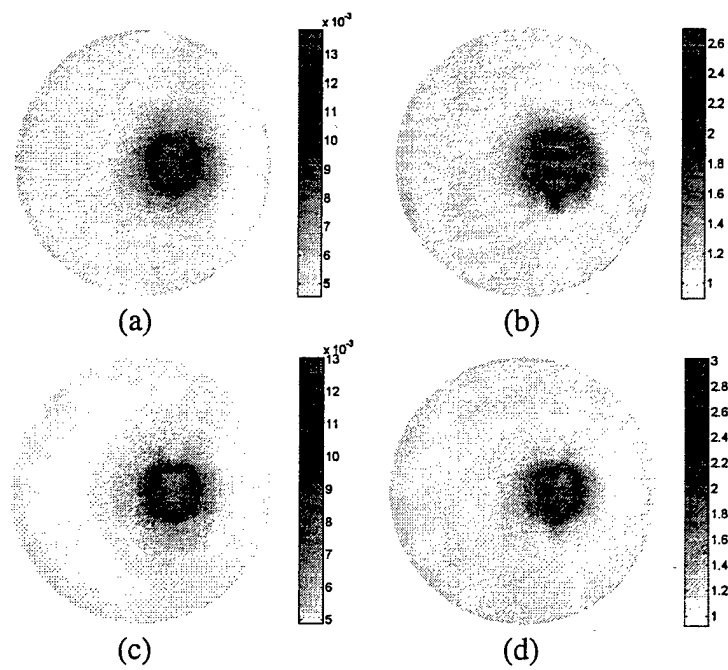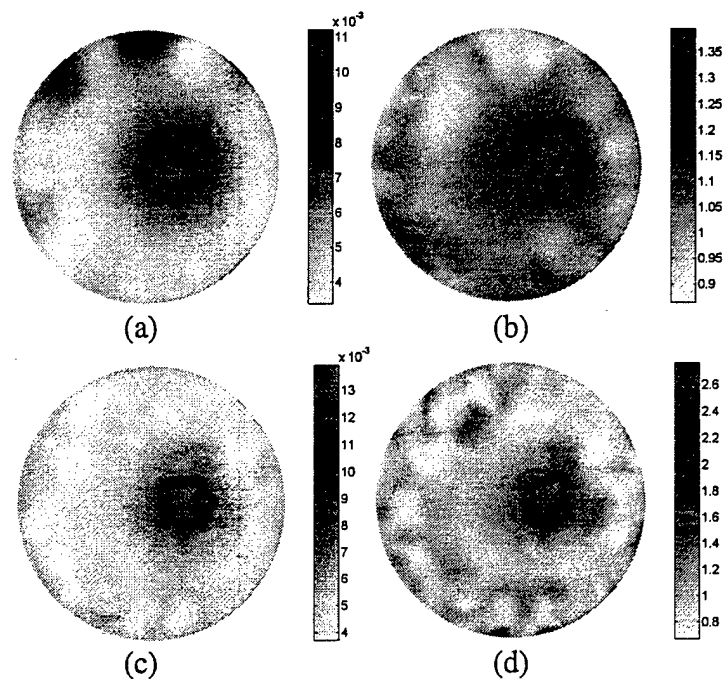
Fig. 2 — Jiang

(a)

(b)

Fig. 3 — Jiang
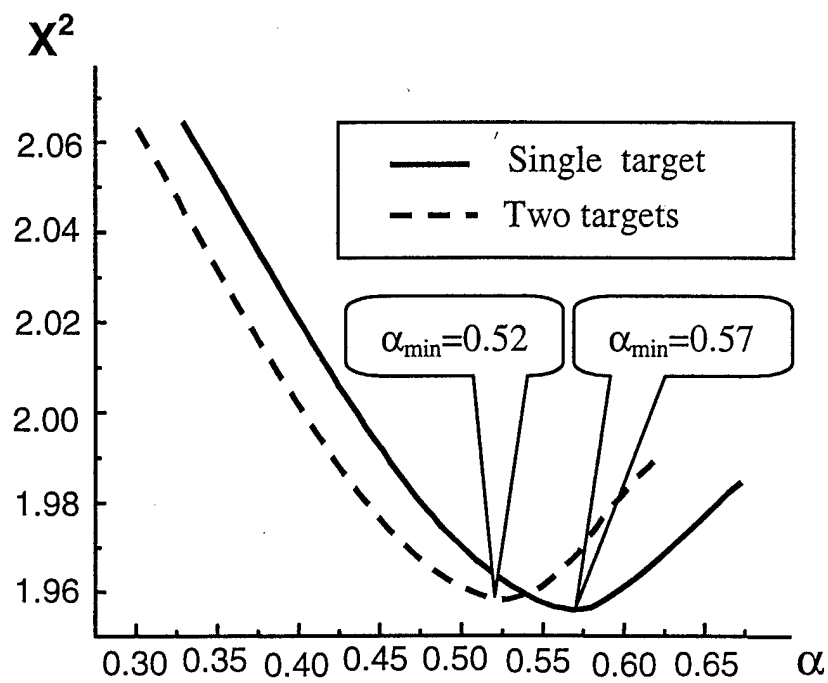
Fig. 4 — Jiang

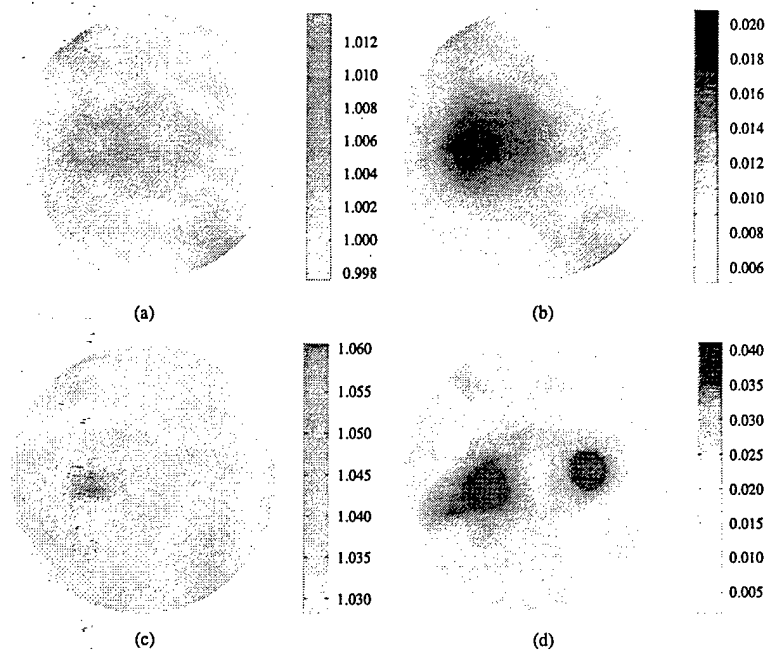(a)　　　　　　　　　　　　　(b)

(c)　　　　　　　　　　　　　(d)

Fig. 5 — Jiang

23

Development of A Combined Optical and Fluorescence Imaging System in Frequency-Domain for Breast Cancer Detection

Nicusor Iftimia, Supeng Liao, and Huabei Jiang

Biomedical Optics Laboratory, Department of Physics & Astronomy
Clemson University, Clemson, SC -USA, 29634-0978
Tel: (864)656-5307   Fax: (864)656-0805   Email: hjiang@clemson.edu

Abstract: We have developed a fully automated frequency-domain system for combined optical and fluorescence reconstruction imaging. The system is currently being evaluated using tissue phantom experiments.

© 1999 Optical Society of America

OCIS Codes: (170.3880) Medical and biological imaging; (170.5270) Photon density waves; (170.3650) Lifetime-based sensing; (110.0110) Imaging systems; (110.6960) Tomography.

We report the design and development of a near-infrared (NIR) frequency-domain system that is be able to provide quantitative optical and fluorescence images of breast tissue. We are presently using phantom experiments to evaluate our system.

Our efforts have been focused on designing a system that can offer high signal-to-noise ratio in order to obtain higher measurements accuracy and thus a good contrast of reconstructed optical/fluorescence images. Because a multiple source-detector arrangement was used, attention was paid to carefully measure the optical transmission over every source-detector path and as well as to the introduction of these corrections in the reconstruction algorithm.

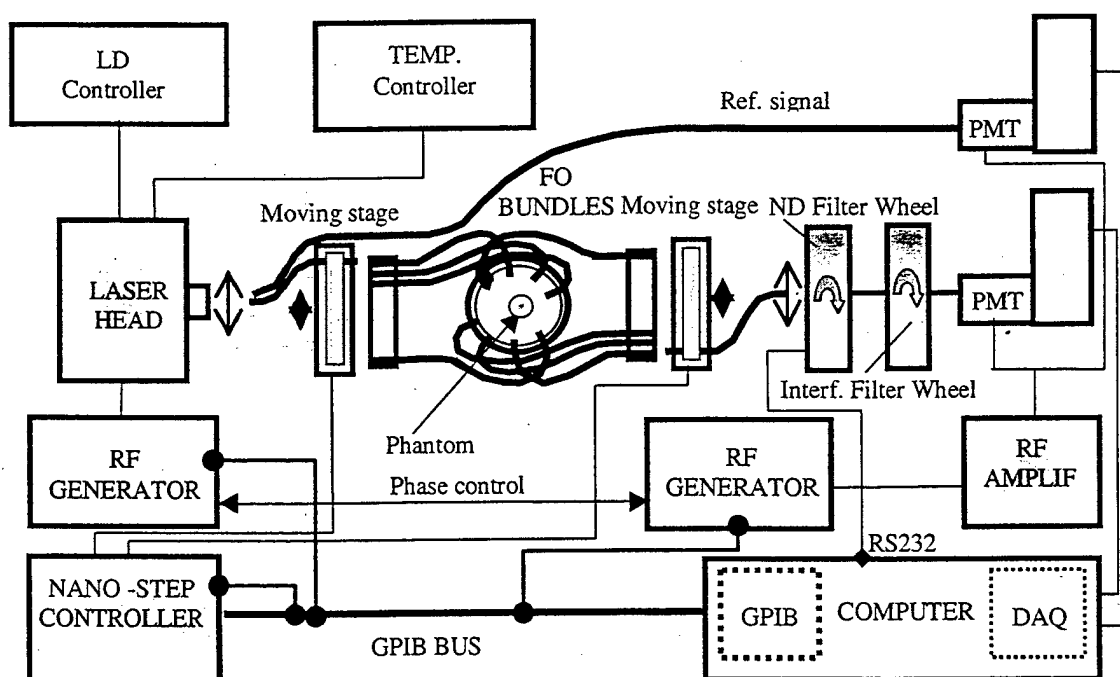Our imaging system is schematically shown Fig. 1.

Fig.1. Schematic diagram of our breast cancer imaging system.

This system employs radio-frequency intensity modulated near-infrared beam from a 60 mW diode laser at 789nm (Mitsubishi). The bias current is modulated at 100 MHz using an IFR 2032A RF Generator (IFR Americas).

The laser beam is sent to the phantom by 16 fiber optic bundles (Fiber Optics, Inc.) with 3 mm inner diameter each, coupled with a high precision Melles Griot moving stage. The diffused radiation is received by the second 16 channel fiber optic bundles and delivered to a PMT (R928 -Hamamatsu Corporation). A second PMT is used to record the reference signal. These photodetectors are supplied at a radio frequency modulated current with 0.1-1KHz shift. The intermediary frequency signal obtained from the PMTs is processed using a DAQ 6032 National Instruments board (16 bits, 100KHz sampling rate). All elements are computer controlled by a GPIB bus. To increase the dynamic range of intensities that the PMT can detect, an automated filter wheel with pre-calibrated neutral density filters is added to the system. Two low pass filters with a cut off of 5 kHz are used to reduce the high frequency noise. AC, DC, and phase shift between reference and probe signals are obtained through the LABVIEW routines.

For every position of the source, 16 measurements for each detector are made, taking alternatively 100 ms samples for fluorescence and nonfluorescence signals. Fluorescence signals are measured using an 830nm interferential filter placed in front of photomultiplier.

Almost simultaneously (10^{-5} sec delay), reference signal is taken in order to measure the phase shift. By using a sample and hold scheme, this time can be reduced at 5 ns and so the errors in the measuring of the phase shift can be further reduced. FFT is used to obtain real and imaginary parts of the reference and probe signals. The total data acquisition time for 256 measurements is about 8 minutes at present time. This acquisition time is long but can be reduced by using a higher speed moving stage or by using a PMT array.

The performance of the system is strongly dependent upon the quality of optical alignment of FO bundles, the characteristics of the modulated light and quality of detectors. Our efforts were directed at obtaining a high signal to noise ratio (SNR) for every position of the detector. In particular, a high DC intensity and a high modulation ratio are very important in order to keep a high SNR. Some optical collimating systems have been used to collect all radiation passing through the ND filters and focusing onto the PMT cathodes.

We have performed measurements for a 50 mm diameter cylindrical solid phantom (0.5% Intralipid +Agar) containing a 7.5 mm diameter target cylinder (0.5% Intralipid + ICG dye + Agar). The measured relative AC and phase shift for both excitation and fluorescence signals are presented in Fig.2. The intensity and phase shift of fluorescence signal are governed by the local fluorescent properties (quantum yield and lifetime). In addition, the fluorescent light that is generated from within the tissue and that propagates to the tissue surface suffers yet another round of attenuation and phase delay as a result of the optical properties of the intervening tissue.
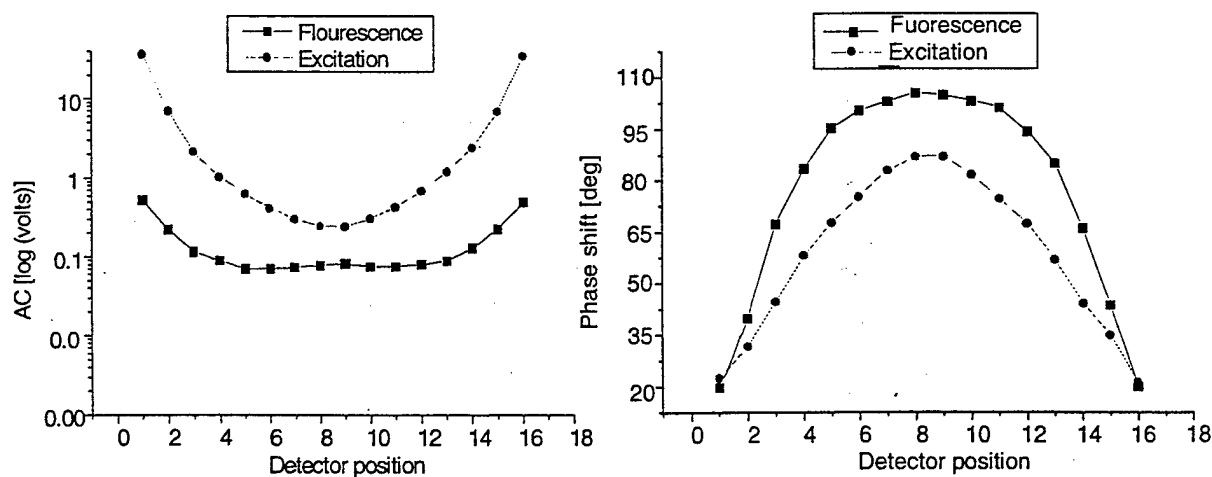

Fig. 2 AC_{rel} and phase shift at different relative position of detector. The fluorescent dye used was ICG.

These measurements have been repeated several times in order to examine the repeatability of the system and to calibrate the system. After the system was calibrated, several sets of 256 measurements were obtained for a cylindrical configuration. Attention was paid to the alignment of axes of the optical fibers that scan the 16 emitting fibers and the 16 receiving fibers. The translation stages that are used to multiplex the fiber optics have a

repeatability of approximately 1μm, allowing a very low variation in the measured signals. The repeatability of the system is approximately 0.5 degree in phase and 0.2 % in AC and DC signals.

The measured excitation and fluorescent data are currently being used to reconstruct both optical and fluorescence images. Our reconstruction algorithms have been described previously in Refs. 1 and 2.

REFERENCES

1. H. Jiang, K. D. Paulsen, Ulf. L. Osterberg, B. W. Pogue, and M. S. Patterson, "Optical image reconstruction using frequency-domain data: simulations and experiments", *J. Opt. Soc. Am. A.* **13**, no. 2, 1996.
2. H. Jiang, "Frequency-domain fluorescent diffusion tomography: a finite element algorithm and simulations", *Appl. Opt.* **37**, 5337-5343(1998).

Fluorescence lifetime tomography of heterogeneous turbid media using frequency-domain measurements

Huabei Jiang*, Ye Yang, and Nicusor Iftimia

Biomedical Optics Laboratory, Department of Physics & Astronomy

Clemson University, Clemson, SC 29634-0978

*Corresponding author

Abstract

We experimentally demonstrate what is believed to be the first simultaneous reconstruction of fluorescence lifetime and yield distributions in heterogeneous turbid media using absolute frequency-domain measurements. The fluorescence images are obtained by use of a finite element based reconstruction algorithm. Experiments are performed using indocyanine green (ICG) dye and tissue-like phantoms in both single- and multi-target configurations.

OCIS Codes: 170.3010, 170.3650, 170.3830, 170.6280, 170.6960

Recently the idea of reconstruction-based fluorescence diffusion tomography has been proposed and developed for clinical applications such as breast cancer detection and tissue functional mapping.[1-5] This new imaging approach relies on the fact that the lifetime and yield of fluorophores in tissue can potentially provide tissue functional information such as tissue oxygenation, pH, and glucose.[6] It is also based on the fact that the fluorophore will preferentially accumulate in tumors, hence providing the best sensitivity for cancer detection.[7] In this type of indirect imaging method, an effective reconstruction algorithm is crucial which allows for the formation of a spatial map of the lifetime and yield of heterogeneous fluorophore distributions. To date fluorescence image reconstructions are largely limited to simulated data, based on linear and nonlinear algorithms.[1-5] Chang et al.[2] attempted to obtain a qualitatively good image of the fluorophore concentration only from dc measurements. In this Letter we present successful quantitative simultaneous reconstruction of both lifetime and yield images from frequency-domain measurements using indocyanine green (ICG) dye and tissue-like phantoms. To our knowledge, the results shown here are the first experimentally reconstructed images for which simultaneous recovery of both lifetime and yield profiles has been achieved with absolute ac excitation and fluorescence data. We show the ability of our algorithm to reconstruct images in which single- and multi-target are embedded in a circular background.

We have used in this study the finite-element based algorithm for reconstruction that has been described in detail in Ref. 5. The algorithm uses a regularized Newton method to update an initial (guess) fluorescent property distribution iteratively in order to minimize an object function composed of a weighted sum of the squared difference between computed and measured data. Here we present a brief overview for context.

In frequency-domain, it is known that propagation of both excitation and fluorescent emission light in tissues or turbid media can be described by the following coupled diffusion equations:[2-5]

$$\nabla \cdot [D_x(r)\nabla\Phi_x(r,\omega)] - \left[\mu_{a_x}(r) - \frac{i\omega}{c}\right]\Phi_x(r,\omega) = -S(r,\omega) \tag{1}$$

$$\nabla \cdot [D_m(r)\nabla\Phi_m(r,\omega)] - \left[\mu_{a_m}(r) - \frac{i\omega}{c}\right]\Phi_m(r,\omega) = -\eta(r)\mu_{a_{x\to m}}\Phi_x(r,\omega)\frac{1+i\omega\tau(r)}{1+\omega^2\tau(r)^2} \tag{2}$$

where $\Phi_{x,m}$ is the photon density for excitation (subscript x) or fluorescent light (subscript m), $D_{x,m}$ is the diffusion coefficient, $\mu_{a_{x,m}}$ is the absorption coefficient due to contributions from both non-fluorescing chromophores and fluorescent dye, $\mu_{a_{x\to m}}$ is the absorption coefficient for the excitation light due to contribution from fluorescent dye, ω is the modulation frequency, c is the velocity of light in the medium, and η and τ are the fluorescent quantum yield and lifetime, respectively. $S(r,\omega)$ is the excitation source term in (1). Note that a single-exponential fluorescence decay has been assumed in the source term for fluorescent light (right-hand-side of (2)); multi-exponential time decay can be handled by a simple extension. The diffusion coefficient can be written as $D_{x,m} = 1/3(\mu'_{s_{x,m}} + \mu_{a_{x,m}})$ where $\mu'_{s_{x,m}}$ is the reduced scattering coefficient. In this study a point excitation source, $S = S_o\delta(r-r_o)$, and Type III boundary conditions (BCs): $-D_{x,m}\nabla\Phi_{x,m} \cdot \hat{n} = \alpha\Phi_{x,m}$, are used, where S_o is the source strength, $\hat{n}$ is the unit normal vector for the boundary surface and α is a coefficient that is related to the internal reflection at the boundary. Both S_o and α are determined directly from the heterogeneous measurements by use of a data pre-processing scheme that has been reported elsewhere.[8]

Making use of finite element discretization, we can obtain two matrix equations for Eqs. (1)-(2) and realize other derived matrix relations through differentiation, which yield a set of equations capable of inverse problem solution:

$$[A_x]\{\Phi_x\} = \{b_x\} \tag{3}$$

$$[A_m]\{\Phi_m\} = \{b_m\} \tag{4}$$

$$[A_m]\left\{\frac{\partial \Phi_m}{\partial \chi}\right\} = \left\{\frac{\partial b_m}{\partial \chi}\right\} - \left[\frac{\partial A_m}{\partial \chi}\right]\{\Phi_m\} \tag{5}$$

$$\left(\mathfrak{I}^T \mathfrak{I} + \lambda I\right)\Delta\chi = \mathfrak{I}^T(\Phi_m^{(o)} - \Phi_m^{(c)}) \tag{6}$$

where the elements of matrices $[A_x]$ and $[A_m]$ are respectively $(a_{x,m})_{ij} = <-D_{x,m}\nabla\psi_j \cdot \nabla\psi_i - (\mu_{a_{x,m}} - \frac{i\omega}{c})\psi_j\psi_i>$, and the entries in column vectors $\{b_{x,m}\}$ and $\{\Phi_{x,m}\}$ are $(b_x)_i = -<S\psi_i> + \alpha\sum_{j=1}^{M}(\Phi_x)_j \oint \psi_j\psi_i ds$,

$(b_m)_i = -<\sum_{k=1}^{K}\eta_k\psi_k\mu_{a_{x\to m}}\sum_{j=1}^{N}(\Phi_x)_j\psi_j\psi_i(1 - i\omega\sum_{l=1}^{L}\tau_l\psi_l)/(1 + \omega^2(\sum_{l=1}^{L}\tau_l\psi_l)^2)> + \alpha\sum_{j=1}^{M}(\Phi_m)_j \oint \psi_j\psi_i ds$,

and $\Phi_{x,m} = \{(\Phi_{x,m})_1, (\Phi_{x,m})_2, \cdots (\Phi_{x,m})_N\}^T$, where $\langle \rangle$ indicates integration over the problem domain, and $\Phi_{x,m}$, τ and η have been expanded as the sum of coefficients multiplied by a set of locally spatially-varying Lagrangian basis functions ψ_j, ψ_l and ψ_k. $\oint$ expresses integration over the boundary surface where Type III BCs have been applied. $(\Phi_{x,m})_i$ is the photon density at node i, N is the node number of a finite element mesh and M is the boundary node number. χ expresses τ or η. $\Phi_m^{(o)}$ and $\Phi_m^{(c)}$ are the observed and computed fluorescent data, respectively. In fluorescence lifetime tomography, the goal is to update the τ and η distributions through the solution of Eqs. (3)-(6) so that a weighted sum of the squared difference between computed and measured data can be minimized.

Our experimental setup used was an automated multi-channel frequency-domain system that was described in detail elsewhere.[9] The system employed a radio-frequency intensity-modulated near-infrared beam. The laser beam at 785 nm was sent to the phantom by 16 fiber optic bundles coupled with a high precision moving stage. The diffused radiation was received by another 16 channel fiber optic bundles and delivered to a PMT. A second PMT was used to record the reference signal. These PMTs were supplied at a radio-frequency modulated current

with 0.1-1KHz shift. The intermediary frequency signal obtained from the PMTs was processed using a National Instruments board. To increase the dynamic range of intensities that the PMT can detect, an automated filter wheel with pre-calibrated neutral density filters was added to the system. For every source position, 16 measurements for each detector were made, taking alternatively 100 ms samples for sample and reference signals. Fluorescence signals were obtained through an 830nm interference filter placed in front of the detection PMT. ac intensity and phase shift between reference and sample signals were obtained using FFT Labview routines. The total data collection time for 256 measurements was 8 minutes.

In our experiments we used a 50 mm diameter solid phantom (0.5% Intralipid +India ink+Agar) as the background medium, making the absorption coefficient $\mu_a = 0.0005/mm$, and the reduced scattering coefficient $\mu'_s = 0.5/mm$. Both single- and two-target configurations were used. The solid targets contained ICG dye with different concentrations (0.5 or 1 μM) plus 0.5% Intralipid and Agar (perfect uptake of the dye was considered here, i.e., no dye was present in the background). The single target had 12.6 or 7.8 mm in diameter, while both targets had 10.3 mm for the two-target case. The 2D finite-element mesh used had 249 nodes and 448 elements for both forward and inverse solutions.

Figs. 1-4 show the reconstructed images of both τ and η and their property profiles along a cut-line crossing the background and target regions for one off-centered target having different target size (Figs. 1 and 2) and different dye concentration (Figs. 1 and 3) and two off-centered targets (Fig. 4). As can be seen, all the targets can be clearly imaged. We also noticed that the recovered images not only are quantitative with respect to the location and size of the target but also quantitatively resolve the values of the lifetime and yield distributions. From Figs. 1-4, we can see that the sharp edges of the target for η images can be recovered, while the target

6

edges are generally broadened for τ images. However, the values of τ images are much more accurately reconstructed than that of η images, as evidenced by the property profiles shown at the bottom of each figure. This is not surprising since normally one would not be able to reconstruct a pure η image from fluorescence diffusion tomography. Instead, one would obtain an image of the product of the yield and absorption coefficient due to the dye.[1-5] Here we have assumed this absorption coefficient to be known as a constant for the entire problem domain. This approximation could be the primary contributor to the inaccuracy of η image recovery. It is also interesting to note that a finite value of τ (larger than the τ value in the target) for the background region is always reconstructed in all the cases studied, although there is no fluorophore distribution in the background.

In summary, we have presented simultaneous reconstruction of both lifetime and yield images in turbid media using ac excitation and fluorescent data. While an ideal, perfect uptake of fluorescent dye in the target has been assumed, this study has clearly demonstrated the feasibility of fluorescence lifetime imaging in turbid media using the reconstruction approach described here. To add fluorophores into the background would primarily challenge our hardware system since the fluorescent signals would be weakened in this case. However, we do not anticipate considerable difficulty to obtain enough signal-to-noise ratio for reconstruction when the fluorophores are present in the background since the dye uptake ratio between the tumor and normal tissue can be as high as 10:1.[4,5,7] In this regard, we plan to conduct experiments in the near future.

References

1. M. O'Leary, D. Boas, X. Li, B. Chance and A. Yodh, *Opt. Lett.* **21**, 158(1996).

2. J. Chang, H. Graber, R. Barbour, *JOSA A* **14**, 288(1997).

3. J. Chang, H. Graber, R. Barbour, *IEEE Trans. Biomed. Engr.* **44**, 810(1997).

4. D. Paithankar, A. Chen, B. Pogue, M. Patterson, E. Sevick-Muraca, *Appl. Opt.* **36**, 2260(1997).

5. H. Jiang, *Appl. Opt.* **37**, 5337(1998).

6. S. Bambot, J. Lakowitz, G. Rao, *Trands Biotechnol.* **13**, 106(1993).

7. E. Sevick-Muraca, G. Lopez, T. Troy, J. Reynolds, C. Hutchinson, *Photochem. and Photobiol.* **66**, 55(1997).

8. H. Jiang, S. Liao, N. Iftimia, *JOSA A* (in press).

9. N. Iftimia, H. Jiang, *Proc. OSA 2000 Biomed. Topical Meetings* (in press).

**Figure Captions**

Figure 1. Reconstructed τ ((a), top) and η ((b), top) images and their property profiles along a cut-line (bottom) of a circular target embedded in the background. The target contained 1 μM of ICG dye and its size was 12.6 mm in diameter. No dye was included in the background. Note that the exact values of τ and η for ICG are 0.58 ns and 0.016 in water, respectively[7]; the exact values of τ and η for the background were assumed to be 2.0 ns and 0.0, respectively.

Figure 2. Reconstructed τ ((a), top) and η ((b), top) images and their property profiles along a cut-line (bottom) of a circular target embedded in the background. All the parameters used here were the same as in Fig. 1 except that the target had 7.8 mm in diameter.
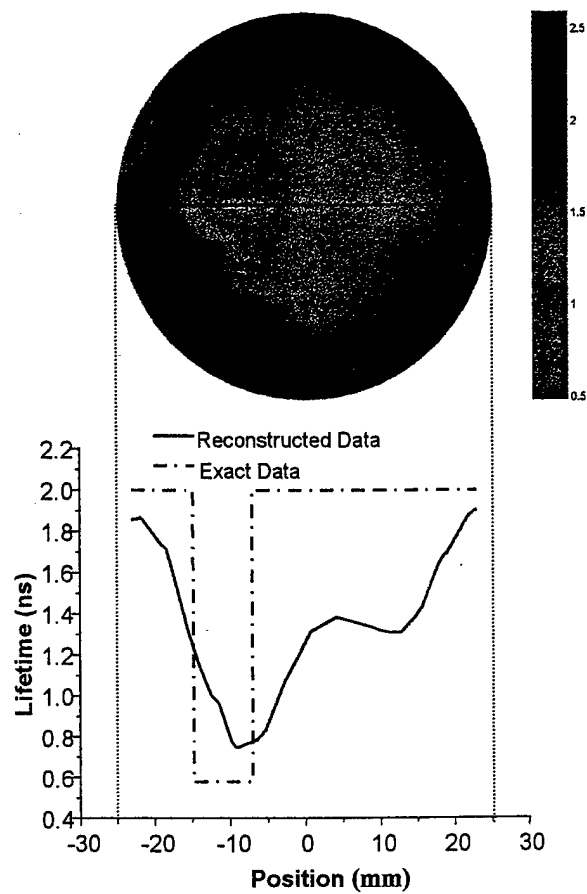
Figure 3. Reconstructed τ ((a), top) and η ((b), top) images and their property profiles along a cut-line (bottom) of a circular target embedded in the background. All the parameters used here were the same as in Fig. 1 except that the target contained 0.5 μM of ICG dye.

Figure 4. Reconstructed τ ((a), top) and η ((b), top) images and their property profiles along a cut-line (bottom) of two circular targets embedded in the background. All the parameters used here were the same as in Fig. 1 except that the targets had 10.3 mm in diameter.
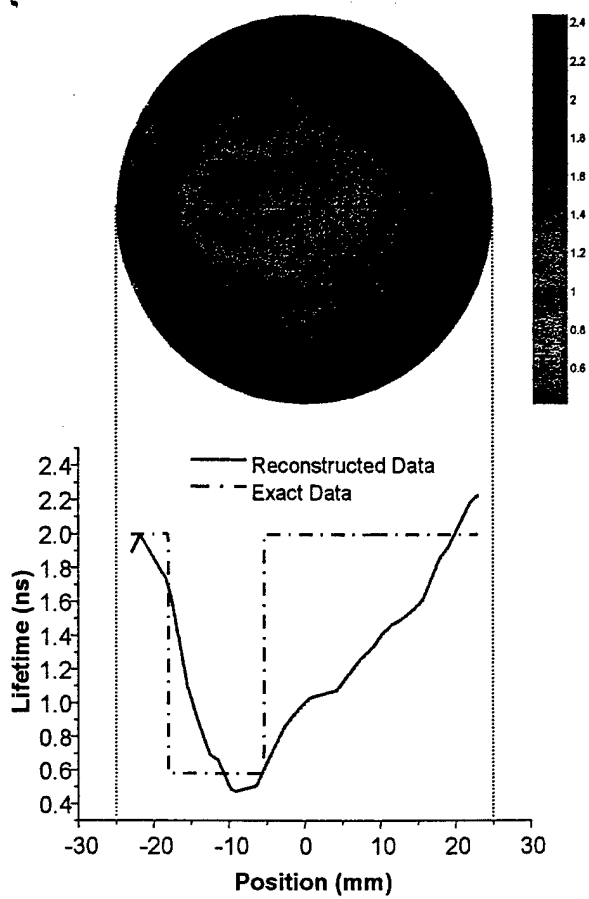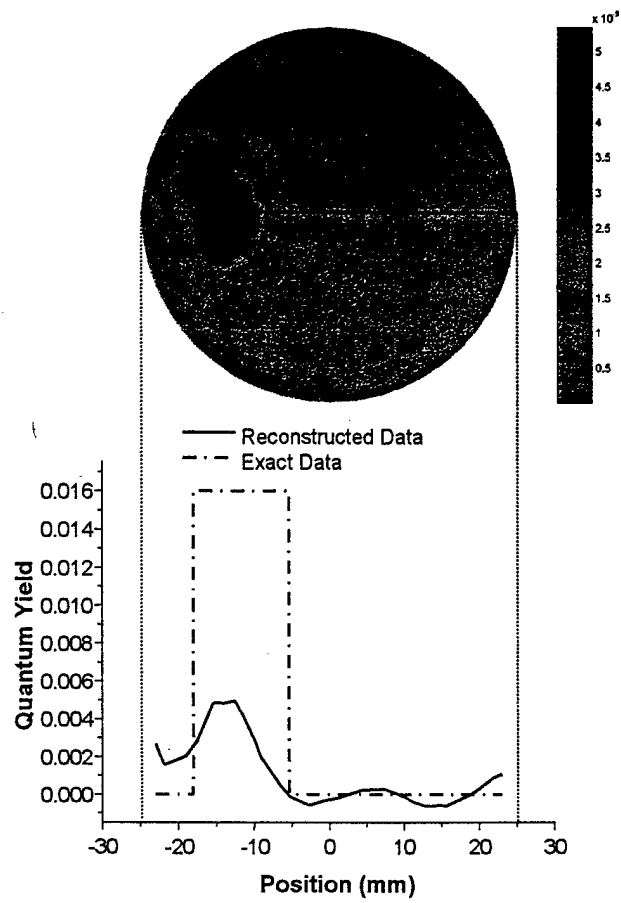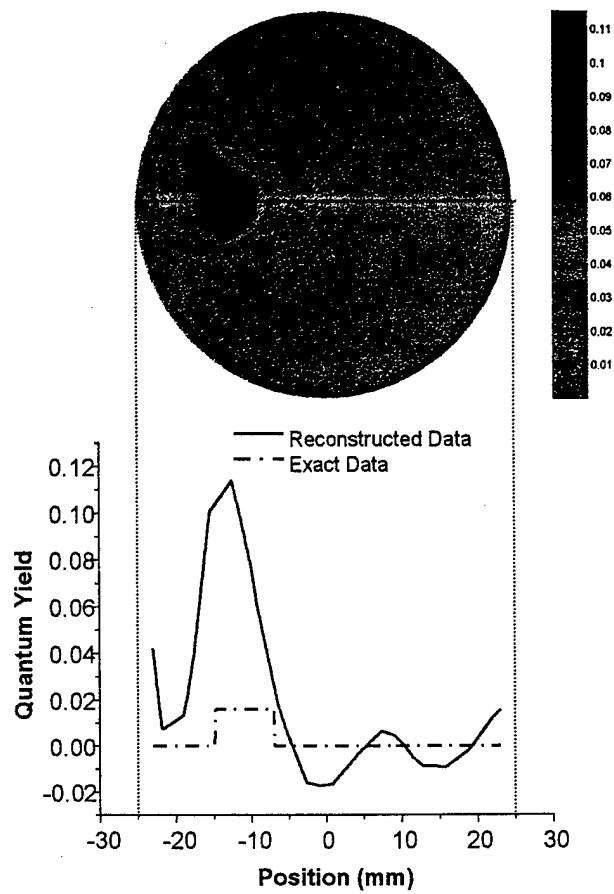
(a)   (b)
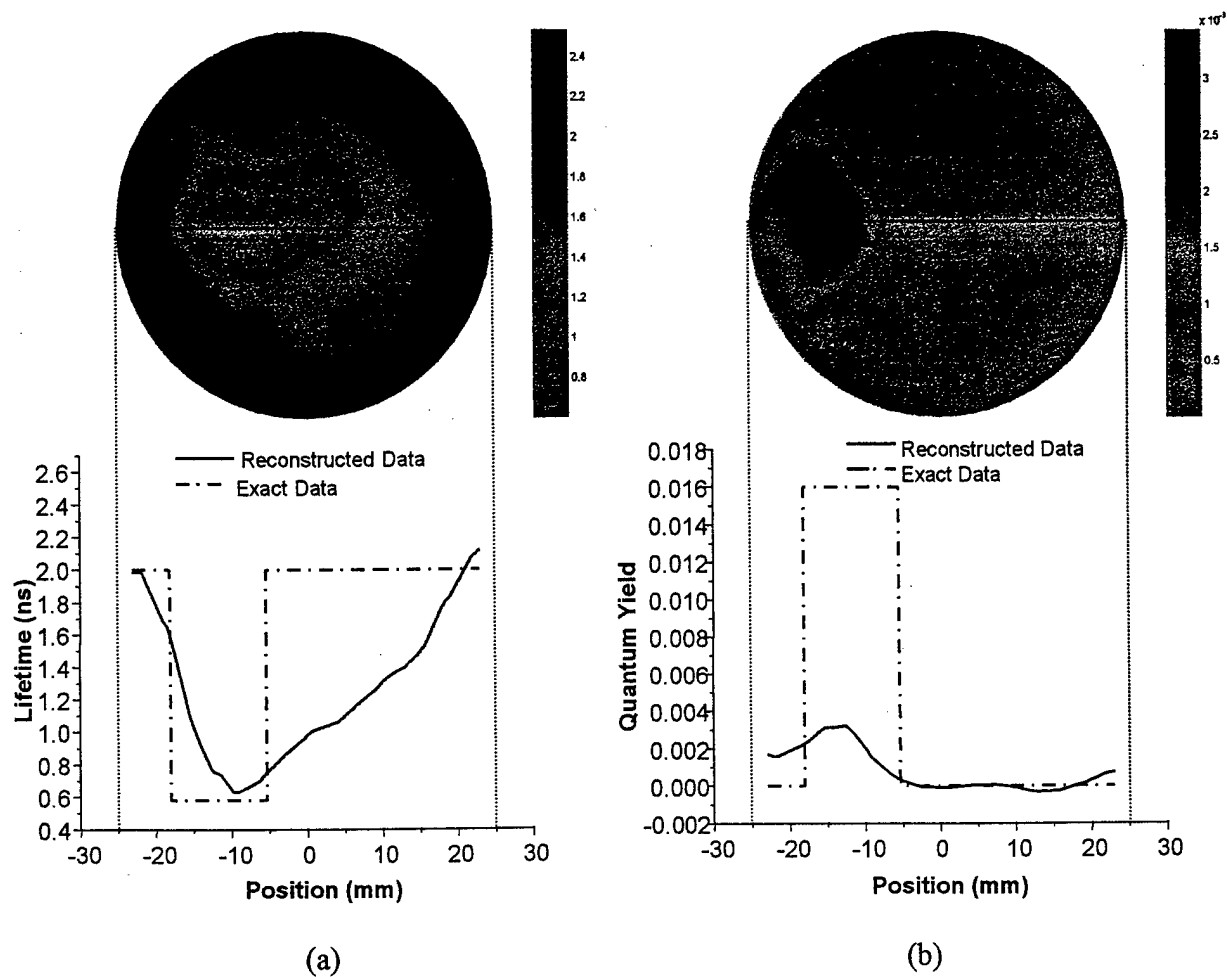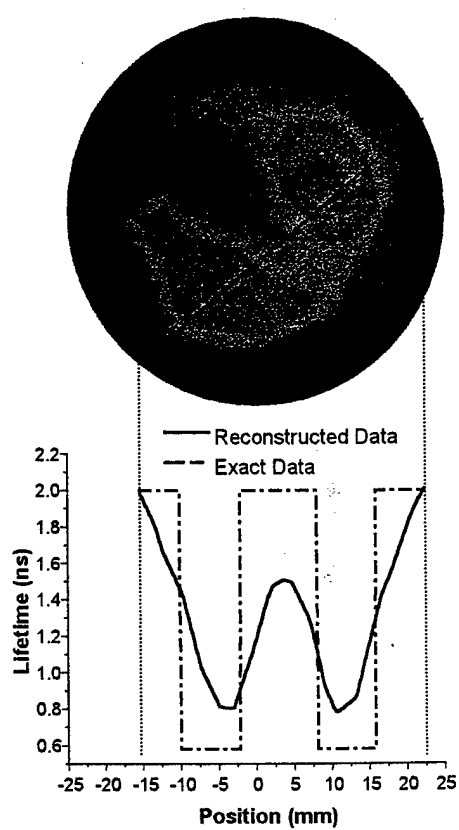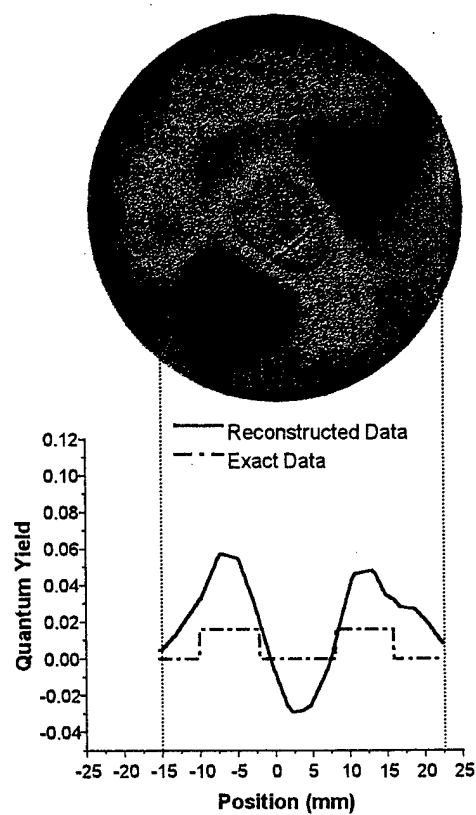
Figure 1--H. Jiang

(a)

(b)

Figure 2--H. Jiang

(a)

(b)

Figure 3--H. Jiang

Figure 4--H. Jiang